The structure of the crust and uppermost mantle beneath the western US revealed by ambient noise and earthquake tomography

Yingjie Yang[1], Michael H. Ritzwoller[1], F.-C. Lin[1], M.P.Moschetti[1], and Nikolai M.Shapiro[2]

1 – Center for Imaging the Earth's Interior, Department of Physics, University of Colorado at Boulder, Boulder, CO 80309-0390, email:yingjie.yang@colorado.edu, phone: 303-735-1850

2 – Institut de Physique du Globe de Paris, CNRS, Paris, France, email: nshapiro@ipp.jussieu.fr

Corresponding author is listed in bold.

Abstract

Ambient noise tomography and multiple plane-wave earthquake tomography are new methods of surface wave analysis that yield much more highly refined information about the crust and uppermost mantle than traditional surface wave techniques. Applied together to data observed at more than 300 broad-band seismic stations from the Transportable Array component of the EarthScope USArray, these methods yield surface wave dispersion curves from 8 to 100 sec period across the entire western US with unprecedented resolution. We use the local Rayleigh wave phase speed curves to construct a unified isotropic 3D Vs model to a depth of about 150 km. Crustal and uppermost mantle features that underlie the western US are revealed in striking relief. As the USArray continues to sweep eastward across the US, the substructure of the entire country will be unveiled.

1 Introduction

The western United States is undergoing broad and diverse deformation caused by strike-slip motion (California plate margin), subduction (Juan de Fuca and Gorda plates beneath the Pacific northwest), extension (Basin and Range province), and large-scale uplift (Colorado Plateau) as well as small-scale lithospheric instabilities (southern Sierra Nevada and Transverse ranges) and a hypothesized continental mantle "plume" (Snake River Plain and Yellowstone). These active tectonic processes are manifest in a variety of crustal and lithospheric structures that have been the subject of intense seismological study using portable seismic instrumentation on a small scale (e.g., Humphreys and Hager, 1990; Boyd et al., 2004; Zandt et al., 2004; Waite et al., 2006; Xue and Allen, 2006) as well as observatory class instrumentation on a continental scale (e.g., van der Lee and Nolet, 1997; Grand, 1994). Traditional P-wave tomography has provided the first tantalizing glimpses at these structures (e.g., Dueker et al., 2001; Burdick et al., 2008; Pollock, 2008) in the mantle and a 3D model has been constructed from ambient noise tomography across the entire US (Bensen et al., 2008), yet no integrated 3D seismological model of the crust and uppermost mantle exists across the western United States on the spatial scale of these features. Such a model is needed to identify the principal structural features across the western US, determine the relations between the features themselves and their surface expressions, and provide clues about their nature and origin.

Recent improvements in seismic instrumentation in the western US coupled with advancements in seismic methodology now allow for the development of such a 3D seismic model of the crust and uppermost mantle beneath the western US. The Earthscope/USArray Transportable Array (TA), presently being deployed across the western US on a nearly uniform 70-km grid, provides the requisite broad-band seismic data (Fig. 1a). The technical innovations in surface wave tomography include ambient noise tomography (e.g., Shapiro et al., 2005; Sabra et al., 2005) and a recent innovation in earthquake tomography that we call teleseismic multi-plane-wave tomography (MPWT). MPWT is a large-scale generalization of the commonly used two-plane-wave method of Yang and Forsyth (2006a, 2006b) and is applied for the first time here. We use these methods together to produce broad-band surface wave dispersion measurements from 8 to 100 sec period that are then interpreted in terms of 3-D shear velocity variations in the crust and uppermost mantle across more than 1.2 x 10^6 km^2 of the western US.

2. Data and Methods

Ambient noise tomography is based on cross-correlating long continuous time series of three-component ambient seismic noise to measure Rayleigh and Love wave group and phase speed curves and the resulting dispersion maps (e.g., Yao et al., 2006; Bensen et al., 2007; Yang et al., 2007; Lin et al., 2007; Cho et al., 2007). The method has been applied across the western US to data from the USArray/TA (Fig. 1a) for time series up to three years in length

to produce phase speed (Lin et al., 2008) and group speed maps from 6 to 40 sec period (Moschetti et al., 2007). The principal advantage of ambient noise tomography is that surface wave dispersion at short periods (<20 sec), which is difficult to measure using teleseismic earthquake methods due to intrinsic attenuation and scattering from distant sources, can be obtained robustly to provide unique constraints on crustal structure.

Information about the mantle is contained in the longer period measurements (>40 sec) obtained from teleseismic earthquakes, but scattering and multi-pathing caused by lateral heterogeneities between the earthquakes and the TA stations distort incoming waves, leading to wavefield complexity. To address this problem, each incoming teleseismic wavefield is fit with a multiple plane wave expansion where each plane wave has an initially unknown amplitude, phase, and propagation direction. This method is a natural extension of the two plane wave method of Yang and Forsyth (2006a, 2006b). Six plane waves are sufficient to model each incoming wavefield across the western US. We interpret the observed phase and amplitude observed across the USArray/TA jointly to model the incoming wavefields and the phase velocity variation across the array. Sixty teleseismic earthquakes are used with Ms > 5.5 and epicentral distances from 30^o to 120^o from the center of the array that occurred in the 21-month period from January 2006 through September 2007. Details about the phase velocity maps are presented by Yang and Ritzwoller (2008) which, however, used a two plane wave method in overlapping sub-regions. Their maps are very similar to those produced with the multiple plane wave generalization.

Ambient noise tomography and teleseismic multiple-plane-wave tomography provide structural information in complementary period bands: ambient noise from 6 to 40 sec and the teleseismic method from 25 to 100 sec. The methods have similar resolution at short and intermediate periods (<40 s), estimated to approach the inter-station spacing (~70 km) at short periods (Fig. 2). In ambient noise tomography, we estimate resolution using the method described by Barmin *et al.* (2001) with modifications presented by Levshin *et al.* (2005). The resolution at a spatial node is defined by a resolution surface, which is a row of the resolution matrix from tomography. To summarize this information, we fit a 2-D symmetric spatial Gaussian function to the surface at each node. Resolution is then defined as twice the standard deviation of the Gaussian fit at each node and this information can be plotted as a resolution map. Examples of resolution maps at 12 and 33 sec period are presented in Figure 2. In the multiple-plane-wave tomography, we do not estimate resolution directly. We infer it indirectly based on the similarity of phase speed maps from these two methods (e.g., Fig. 3f).

In ambient noise tomography (ANT), uncertainties in the dispersion measurements are determined by repeating the measurements over disjoint time intervals (e.g., Bensen et al., 2007). Uncertainties at different nodes in the dispersion maps, however, are estimated using a new method of tomography called Eikonal tomography (F. Lin, M.H. Ritzwoller, R.Snieder, manuscript in preparation, 2008). This method involves wavefield phase time tracking and the production of a phase travel time map centered on each station. Each station-centered

phase-time map is interpreted separately with the Eikonal equation (e.g., Kravtsov and Orlov, 1990) to estimate local phase speed from the modulus of the local gradient of the phase-time map. Rayleigh wave uncertainties are estimated at a given location from the multiplicity of phase-time maps centered on different stations. Uncertainties average 5 - 10 m/s near the center of the study region but increase near its periphery. In multiple-plane-wave tomography, standard errors are taken from the model covariance matrix (Yang and Forsyth, 2006a) and average between 10-15 m/sec near the center of the region but grow near the edges.

Used in combination, ambient noise and multi-plane wave tomography provide Rayleigh wave phase speed maps from 8 to 100 sec period (Fig. 3), a band sensitive to depths from the surface to about 160 km. In the overlapping period range (25-40 sec), the methods produce similar phase speed measurements over most of the study area except near the borders where station coverage is not ideal (Figure 3d, e and f), and we average the measurements.

3. Model Construction

The set of Rayleigh wave phase speed maps is inverted for a 3D isotropic shear velocity (Vs) model on a $0.5^{o}\times0.5^{o}$ geographic grid using a two-step procedure. Because only Rayleigh waves are used in the inversion, the primary sensitivity is to Vsv and we have no Vsh information. Thus, although we will refer to the model as a Vs-model, it is in fact Vsv. At each point on the grid, the local Rayleigh wave phase speed curve is constructed from the

dispersion maps and this curve provides the data for the inversion.

The first step is a linearized inversion of the Rayleigh wave phase speed curve for the best fitting Vs-model below the grid point. In the linearized inversion, depth-dependent shear wave speeds are parameterized in eleven constant Vs layers from the Earth's surface to 200 km depth with three layers for the crust and eight layers for the upper mantle. Because Rayleigh wave phase speeds depend primarily on Vs, we scale Vp to Vs using a constant Vp/Vs ratio of 1.735 in the crust and 1.756 in the mantle (Chulick and Mooney, 2002). Due to the trade-off between Moho depth and Vs in the two layers adjacent to Moho, we fix crustal thickness to that derived from receiver functions (Gilbert and Fouch, 2008).

In the second step, a Markov Chain Monte-Carlo resampling of model space (Shapiro and Ritzwoller, 2002; Bensen et al., 2008; Yang et al., 2008) is performed to quantify the uncertainty in shear velocity versus depth. The Markov Chain Monte-Carlo inversion executes a random walk through model space in the neighborhood of the model derived from the linearized inversion. At each spatial node, this generates an ensemble of "acceptable" 1D shear velocity models that fit the Rayleigh wave dispersion curve within specified uncertainties. To expedite model space sampling, the velocities in the crust and upper mantle are allowed to vary within a ±5% range of the initial model, a range similar to the variation of S-wave speed across the study region. The thicknesses of the upper and middle crustal layers are fixed, but the thickness of the lower crust (and hence Moho depth) is allowed to

vary from the initial model within ±5 km. If the predicted dispersion curve for a candidate model matches the measured curve with an average misfit of less than twice the data standard deviation, the model is retained and termed "acceptable". Further details about the Monte-Carlo inversion can be found in Shapiro and Ritzwoller (2002) and Bensen et al. (2008).

For each grid point, the average of the resulting ensemble of acceptable models at each depth is taken as the expected value of the Vs-model and the half-width of the corridor of the ensemble provides an estimate of model uncertainty (Fig.1b). To visualize the uncertainty in the 3D model we use the notion of "persistent features" (Shapiro and Ritzwoller, 2002). An anomaly relative to the average model across the region is considered to be "persistent" if it appears in every member of the ensemble of acceptable models; that is, if its value is greater than the half-width of the corridor of models. Acceptability is defined relative to the dispersion measurement uncertainties, which average 5-10 m/s at periods from 8 to 25 sec and 10-15 m/s at periods from 30 to 100 sec. The final model is isotropic and is composed of three crustal layers and five B-spline functions in the upper mantle to represent mantle velocity to a depth of 200 km. Vs is constrained to increase with depth monotonically in the crust and vary with depth smoothly in the mantle. An example of the output from the process at a single location is plotted in Figure 1b and 1c.

4. The 3D Model: Discussion

The inversion method is applied across the far western US, including all of California, Oregon, Washington, and the western half of Idaho. The period-averaged misfit to the dispersion measurements by the 3D Vs model is about 10-15 m/s across most of the study area (Fig. 4). The average uncertainties of the 3D Vs model, defined as the standard deviation among the ensemble of acceptable model averaged over the study region, are about 1% in the upper and middle crust and in the mantle below 50 km (Fig. 5i) and somewhat larger near the Moho discontinuity due to the trade-off of Moho depth with Vs in neighboring depths. These values are about two to three times smaller than the RMS of the shear velocity anomalies at the same depth (Fig. 5i). Below about 160 km depth, the RMS of the recovered anomalies crosses over the uncertainty of the model. We, therefore, interpret features of the recovered model only above about 160 km.

The resulting 3D Vs model (Fig. 5) with uncertainties shown in Figure 6 reveals a wealth of structural information correlated closely with regional geological features and tectonics. In the crust, shear velocity anomalies typically are similar with depth, except beneath the principal sedimentary basins such as the Central Valley of California, the Salton Trough in the Imperial Valley, the Los Angeles Basin, and the Columbia River Basin (Yakima Fold Belt) near the Washington – Oregon border. These basins exhibit pronounced low shear wave speeds in the upper crust due to the slowness of the sediments. Low wave speeds are also

observed along the Coast Ranges from California through Washington due to continuous deformation in California along the San Andreas fault, south of the Mendocino Transform, and the accumulation of off-scraped and metamorphosed sediments resulting from past and ongoing subduction north of the transform. The most significant difference between velocity anomalies in the upper and the middle/lower crusts (10 km – Moho) (Fig. 5b) is that high velocities underlie the principal sedimentary basins, which is qualitatively consistent with crustal isostasy. Throughout the crust, shear wave speeds are high in the Sierra Nevada and the Peninsular Ranges which are composed primarily of higher velocity granitic batholiths. The non-granitic Cascade Range is characterized by nearly average wave speeds. Modest low velocities are observed throughout the Basin and Range province, probably due to elevated crustal temperatures resulting from relatively thin lithosphere (Zandt et al., 1995). The northern Columbia Plateau and the western Snake River Plain are characterized by high wave speeds throughout the entire crust, presumably caused by compositional heterogeneity resulting from igneous intrusions related to basalt flows (Peng and Humphreys, 1998; Hales et al. 2005).

In the upper mantle (Fig. 5c, d), velocity anomalies are distinct from those observed in the overlying crust, reflecting decoupling between the crust and upper mantle. Three sets of prominent high velocity features are observed, respectively, beneath (1) the Cascade Range associated with subduction of oceanic lithosphere, (2) the southern Great Valley of California and the Transverse Range associated with lithospheric instability, and (3) eastern Washington

and the northern Rocky Mountains associated with thick, stable Proterozoic lithosphere. The high velocity lithosphere of the subducting Juan de Fuca and Gorda plates has an apparent thickness of 50-60 km (Fig. 5e and 5f), consistent with its relatively young age, and persists to a depth greater than our resolvable depth of ~160 km. The edge of the high velocity slab is seen as a sharp north-south velocity contrast near the Mendocino Transform (Fig. 5d), coincident with the location of the southern edge of the Gorda plate. High velocity anomalies in southern California are consistent with previous surface wave studies (e.g., Yang and Forsyth, 2006a, 2006b) and regional P-wave tomography (Humphreys and Clayton, 1990), and have been interpreted as lithospheric downwellings or "drips" caused by a Rayleigh-Taylor instability (Humphreys and Hager, 1990; Biasi and Humphreys, 1992; Zandt and Carrigan, 1993). The lithospheric "drip" beneath the southern Central Valley can be seen to reach a depth of 120-150 km (Fig. 5g, Profile C-C'), which is somewhat deeper than that beneath the Transverse Range. High wave speeds beneath the northern Rocky Mountains extend deeper than 160 km (Fig. 5e), which implies that the Proterozoic lithosphere there was not completely eroded by past tectonic events such as the Laramide Orogeny, consistent with earlier P-wave tomography (e.g., Dueker et al., 2001).

Slow mantle wave speeds are imaged beneath the Cascadia arc of northern California, Oregon, and Washington, above and to the east of the subducting Juan de Fuca and Gorda plates. These low wave speeds reflect the influence of subduction on the overlying mantle wedge and perhaps also the interaction between a continental plume (the Yellowstone plume)

and the upper mantle. In the northern part of the arc (Fig. 5e, profile A-A'), low speeds are confined to the mantle wedge overlying the subducting plate with the lowest speeds directly underlying recently active Cascade volcanoes (Mt. St. Helens, Mt. Hood). These low wave speeds are coincident with the source volume of the volcanic magmas and may be caused by partial melting produced when volatiles released from the subducting slab rise into the overlying upper mantle (Peacock, 1990). In contrast, in southern Oregon (Fig. 5f, profile B-B') low wave speeds extend much further east, underlying the extensive extrusive volcanism of the high lava plains of southern Oregon and the northern Basin and Range province. This broad low velocity anomaly, appearing at depths above ~120 km, probably reflects high temperatures in the upper mantle (Camp and Ross, 2004). The warm lithosphere in this region encompasses both the Yellowstone and Newberry hotspot tracks, but is much broader and may reflect plume-fed asthenospheric flow (Yamamoto and Morgan, 2007) following the impact of the mantle plume head beneath the lithosphere that occurred near the boundary of Oregon and Nevada at ~16.6 Ma (Camp and Ross, 2004; Xue and Allen, 2007). As the Yellowstone plume moved northeast relative to the North American plate to its current location beneath Yellowstone, low velocities imprinted the upper mantle along the Snake River Plain (Saltzer and Humphreys, 1997). The low wave speeds observed in the mantle beneath the western Snake River Plain slow further toward the east (Fig. 5f), as the date of the last volcanic event approaches the present. Low seismic waves speeds also underlie the Basin and Range province, but are weaker and may reflect lithospheric thinning consistent with the buoyant upwelling of asthenospheric material in response to the

detachment of the Farallon plate in the post-Laramide era from ~ 50 to 20 Ma (Humphreys et al., 2003).

5. Conclusions

This study merges new methods in seismic imaging using surface waves with a new kind of seismic array, the extensive broad-band Transportable Array component of EarthScope/USArray. Ambient noise tomography (ANT) and multiple plane-wave tomography (MPWT) provide higher resolution information than traditional methods of surface wave tomography, with ANT producing information about the crust and uppermost mantle and MPWT generating information about the mantle. Used together, these methods deliver dispersion curves across the western US from 8 to 100 sec period, which impose constraints on the crust and uppermost mantle to a depth of about 150 km. Inversion of these Rayleigh wave phase speed curves with a Markov Chain Monte Carlo method generates an isotropic 3D model with attendant uncertainties. The structural features that result cohere with known geological structures. Future advancements will result from incorporating Love waves and other kinds of seismic information and investigating the generalization of the model to include low velocity zones in the crust (if needed) and anisotropy.

By the year 2012, the USArray/TA will have been moved systematically across the conterminous United States. The application of the methods presented in this paper to these data promises to continuously reveal structural images of the crust and uppermost mantle

across the entire US in previously unprecedented detail.

Acknowledgments: All data used were obtained from the IRIS Data Management Center. The authors are grateful to Hersh Gilbert for providing his crustal thickness map prior to publication. This research was supported by NSF grants EAR-0450082 and EAR-0711526.

References:

Barmin, M.P., Ritzwoller, M.H. and Levshin, A.L. (2001). A fast and reliable method for surface wave tomography, *Pure appl. Geophys.,* 158, 1351–1375.

Bensen, G. D., M. H. Ritzwoller and Y. Yang (2008), A 3D velocity model of the crust and uppermost mantle beneath the United States from ambient seismic noise, submitted to *Geophys. J. Int.*

Bensen, G.D., M.H. Ritzwoller, M.P. Barmin, A.L. Levshin, F. Lin, M.P. Moschetti, N.M.Shapiro, and Y. Yang (2007), Processing seismic ambient noise data to obtain reliable broad-band surface wave dispersion measurements, *Geophys. J. Int.*, 169, 1239-1260.

Biasi, G. P., and E. D. Humphreys (1992), P-wave image of the upper mantle structure of Central California and southern Nevada, *Geophys. Res. Lett.*, 19, 1161-1164, 1992.

Boyd, O. S., C. H. Jones, and A. F. Sheehan (2004), Foundering lithosphere imaged beneath the southern Sierra Nevada, California, USA, *Science*, 305, 660–662.

Burdick, S., Li, C., Martynov, V., Cox, T., Eakins, J., Astiz, L, Vernon, F.L., Pavlis, G.L., Van der Hilst, R.D. (2008), Upper mantle heterogeneity beneath North America from travel time tomography with global and USArray transportable array data, *Seismological Research Letters*, 79,384-392,.

Camp, V. E., and M. E. Ross (2004), Mantle dynamics and genesis of mafic magmatism in the intermontane Pacific Northwest, *J. Geophys. Res.*, *109*, B08204, doi:10.1029/2003JB002838.

Cho, K. H., R. B. Herrmann, C. J. Ammon, and K. Lee (2007), Imaging the upper crust of the Korean Peninsula by surface-wave tomography, *Bull. Seismol. Soc. Am.*, 97(1B), 198–207.

Chulick, G. S., and W. D. Mooney (2002), Seismic structure of the crust and uppermost mantle of North America and adjacent oceanic basins: A synthesis, *Bull. Seis. Soc. Am.*, 92 (6), 2478-2492.

Dueker K, Yuan H, and Zurek B (2001), Thick-Structured Proterozoic Lithosphere of the Rocky Mountain Region. GSA Today, 11(12), 4–9.

Gilbert, H. and M.J. Fouch, Complex Upper Mantle Seismic Structure Across the Southern Colorado Plateau / Basin and Range II: Results from Receiver Function Analysis, *Eos*

Trans. AGU 88, S41B-0558, 2008.

Grand, S. P.(1994), Mantle shear structure beneath the Americas and surrounding oceans, *J. Geophys. Res.*, *99*, 11,591-11,621.

Hales, T.C., D. Abt, E. Humphreys, and J. Roering (2005), A lithospheric instability origin for Columbia River flood basalts and Willowa Mountains uplift in northeast Oregon, *Nature*, *438*, 842-845.

Humphreys, E., E. Hessler, K. Dueker, E. Erslev, G. L. Farmer, and T. Atwater (2007), How Laramide-age hydration of North America by the Farallon slab controlled subsequent activity in the western U.S., *The George A. Thompson volume, International Book Series, 7* (invited), S. L. Klemperer and W. G. Ernst, editors, 524-544, Geol. Soc. Am., Boulder Colorado, 2003

Humphreys, E.D. and Hager, B.H. (1990), A kinematic model for the late Cenozoic development of southern California crust and upper mantle, *J. geophys. Res.*, 95, 19,747–19,762.

Humphreys, E.D., and R.W. Clayton (1990), Tomographic image of the southern California mantle, *J. Geophys. Res*., 95, 19725-19746.

Kravtsov, Y.A. and Y.I Orlov, *Geometrical Optics of Inhomogeneous Media*, Springer-Verlag, New York, 1990.

Levshin, A.L., Barmin, M.P., Ritzwoller, M.H. and Trampert, J. (2005), Minorarc and major-arc global surface wave diffraction tomography, *Phys. Earth planet. Ints.,* 149, 205–223.

Lin, F., M. H. Ritzwoller, J. Townend, M. Savage, and S. Bannister (2007), Ambient noise Rayleigh wave tomography of New Zealand, *Geophys. J. Int.*, 170(2), doi:10.1111/j.1365-246X.2007.03414.x.

Lin, F., M.P. Moschetti, and M.H. Ritzwoller (2008), Surface wave tomography of the western United States from ambient seismic noise: Rayleigh and Love wave phase velocity maps, *Geophys. J. Int.*, doi:10.1111/j1365-246X.2008.03720.x.

Moschetti, M. P., M. H. Ritzwoller, and N. M. Shapiro (2007), Surface wave tomography of the western United States from ambient seismic noise: Rayleigh wave group velocity maps, *Geochem. Geophys. Geosyst.*, 8, Q08010, doi:10.1029/2007GC001655.

Peacock, S.M. (1990), Fluid processes in subduction zones, *Science*,248,329-337..

Peng, X., and E. Humphreys (1997), Crustal velocity structure of northwest Nevada from teleseismic receiver function analysis, *Bull. Seis. Soc. Am., 87*, 745-754.

Pollitz, F. (2008), Observations and interpretation of fundamental-model Rayleigh wavefields recorded by the Transportable Array (USArray), *J. Geophys. Res,* in press.

Sabra, K. G., P. Gerstoft, P. Roux, W. Kuperman, and M. C. Fehler (2005),Surface wave tomography from microseisms in Southern California, *Geophys. Res. Lett.*, 32, L14311, doi:10.1029/2005GL023155.

Saltzer, R., and E. Humphreys (1997), Upper mantle P wave velocity structure of the eastern Snake River Plain and its relationship to geodynamic models of the region, *J. Geophys. Res*., 102(B6), 11829-11841.

Shapiro, N.M. and M.H. Ritzwoller (2002), Monte-Carlo inversion for a global shear velocity

model of the crust and upper mantle, *Geophys. J. Int.*, 151, 88-105.

Shapiro, N.M. M. Campillo, L. Stehly, and M.H. Ritzwoller (2005), High resolution surface wave tomography from ambient seismic noise, *Science*, 307, 1615-1618.

Van der Lee, S. and G. Nolet (1998), Upper mantle S velocity structure of North America, *J. Geophys. Res.* 102 , 22815-22838.

Waite, G.P., R.B. Smith, and R.M. Allen (2006), Vp and Vs structure of the Yellowstone hot spot: evidence for an upper mantle plume, *J. Geophys. Res., 111*, B04303, doi:10.1029/2005JB003867

Xue, M., and R. M. Allen (2007), The fate of the Juan de Fuca plate: Implications for a Yellowstone plume head, *Earth Planet. Sci. Lett.*, 264, 266–276, 2007.

Yamamoto M, J.P. Morgan and W.J. Morgan (2007), Global plume-fed asthenosphere flow—I: Motivation and model development. Special Paper 430: *Plates, Plumes and Planetary Processes,* 430, 165–188.

Yang, Y., A. Li, M. H. Ritzwoller (2008), Crustal and uppermost mantle structure in southern Africa revealed from ambient noise and teleseismic tomography doi:10.1111/j.1365-246X.2008.03779.x

Yang, Y., and D.W. Forsyth (2006a), Rayleigh wave phase velocities, small-scale convection and azimuthal anisotropy beneath southern California, *J. Geophys. Res.*, 111, B07306, doi:10.1029/2005JB004180.

Yang, Y., and D.W. Forsyth (2006b), Regional tomographic inversion of amplitude and phase of Rayleigh waves with 2-D sensitivity kernels, *Geophys. J. Int.,* 166, 1148-1160.

Yang, Y., and M. H. Ritzwoller (2008), Teleseismic surface wave tomography in the western U.S. using the Transportable Array component of USArray, *Geophys. Res. Lett.*, 35, L04308, doi:10.1029/2007GL032278.

Yang, Y., M. H. Ritzwoller, A. L. Levshin, and N. M. Shapiro (2007), Ambient noise Rayleigh wave tomography across Europe, *Geophys. J. Int.*, 168(1), 259– 274.

Yao, H., R. D. van der Hilst, and M. V. de Hoop (2006), Surface-wave array tomography in SE Tibet from ambient seismic noise and two-station analysis-I. Phase velocity maps, *Geophys. J. Int.*, 166(2), 732– 744.

Zandt, G. and C. R. Carrigan (1993). Small-scale convective instability and upper mantle viscosity under California,*Science* 261, 460-463.

Zandt, G., H. Gilbert, T. J. Owens, M. Ducea, J. Saleeby, and C. H. Jones (2004), Active foundering of a continental arc root beneath the southern Sierra Nevada in California, *Nature*, 431, 41– 46.

Zandt, G., S. C. Myers, and T. C. Wallace (1995), Crust and mantle structure across the Basin and Range-Colorado Plateau boundary at 37°N latitude and implications for Cenozoic extensional mechanism, *J. Geophys. Res.*, *100*(B6), 10,529–10,548.

Figure Captions:

Figure 1. **(a)** Station used in this study (west of 114°W). The principal large-scale geological features of the western United States are identified, including the Cascade Range (CR), the Columbia River Flood Basalts (CRFB), the Rocky Mountains (RM), the High Lava Plains (HLP), the Snake River Plain (SRP), the Great Valley (GV), the Sierra Nevada Range (SN), the Basin and Range province (BR), the Transverse Range (TR), the Peninsular Range (PR), and the Salton Trough (ST). Triangles mark the locations of the EarthScope TA seismic stations used in this study. The red lines outline the boundaries between major tectonic units. (b) & (c) An example of the Monte-Carlo inversion for the point identified by the red star in the Basin and Range province in Fig.1a. (b) The resulting ensemble of acceptable Vs models (gray lines) and the average of the ensemble (red line). (c) Gray lines are predicted dispersion curves from the ensemble of Vs models shown in Fig. 1b. The dark grey line is the observed dispersion curve with error bars at individual periods.

Figure 2. Resolution maps from ambient noise tomography for Rayleigh wave phase speed at periods of 12 and 33 sec. Resolution is defined as twice the standard deviation of a 2-D Gaussian function fit to the resolution matrix at each point (16). The 70 km resolution contour is shown with a thick black line. Resolution at other periods is similar.

Figure 3. (a-d) Rayleigh wave phase speed maps derived from ambient noise tomography (ANT) at periods of 8, 16, 25, and 33 sec, and (e,g-i) teleseismic multiple-plane-wave tomography (MPWT) at 33, 50, 66, and 100 sec. The 100 km resolution contour (the bold gray contours) is plotted for reference on the ANT maps. (f) The difference between the phase speeds determined by ANT and MPWT at 33 sec period. Anomalies are presented as the percent deviation from the average speed across the region.

Figure 4. Period-averaged misfit map presenting the average of the difference between the observed dispersion curves and the curves computed from the 3D Vs model. Largest misfit occurs west of the Cascade Range where the ambient noise and multiple plane wave earthquake tomography are most discordant in the period band of overlap (Fig. 3f).

Figure 5. (a)-(d) Shear wave speed maps at depths of 5, 15, 50 and 100 km. (e)-(g) Vertical cross sections of shear wave speed along three profiles delineated by the white lines in Fig. 3d. Black contours outline the "persistent" upper mantle velocity anomalies. Topography is over-plotted above individual cross sections with major tectonic units labeled using abbreviations defined in Fig. 1 caption. The black triangles in (c)-(f) represent active volcanoes in the Cascade Range. Shear velocity anomalies are computed relative to the average 1D model plotted in (h). (i) The standard deviation of the ensemble of acceptable models (i.e., average uncertainty, dashed line) and the root mean square (RMS) of the velocity perturbations (solid line) taken across the entire region.

Figure 6. Maps of the estimated uncertainty of the 3D Vs model derived from the ensemble of acceptable models produced by the Monte-Carlo inversion at the depths of 5, 15, 50 and 100 km. Largest uncertainties are in the lower crust and uppermost mantle due to trade-off between Moho depth and Vs in adjacent layers.

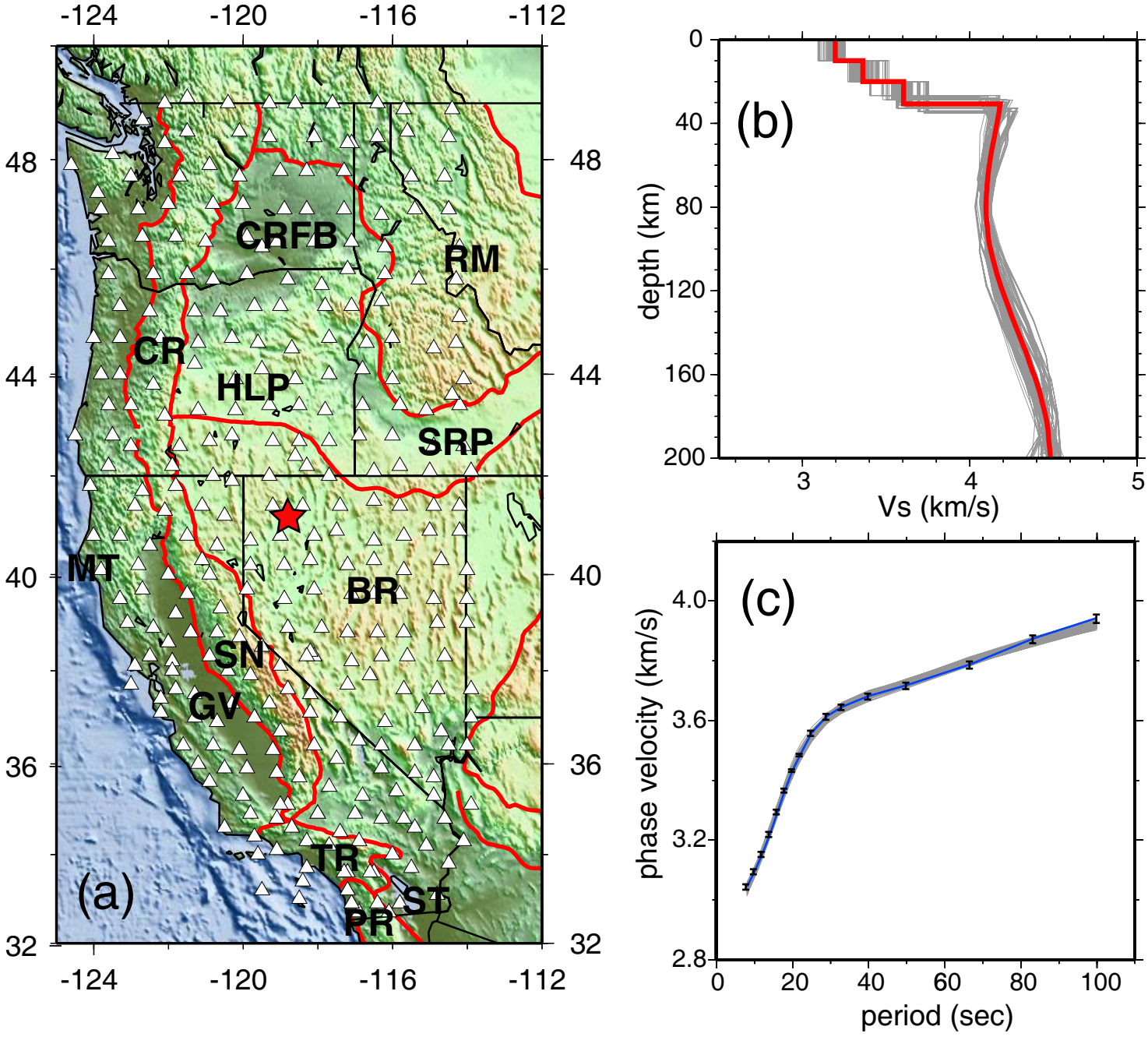
-124
-120
-116
-112
48
44
40
36
32
CRFB
RM
CR
HLP
SRP
MT
BR
SN
GV
TR
PR
ST
(a)
(b)
depth (km)
0
40
80
120
160
200
3
4
5
Vs (km/s)
(c)
phase velocity (km/s)
4.0
3.6
3.2
2.8
0
20
40
60
80
100
period (sec)

Figure 1

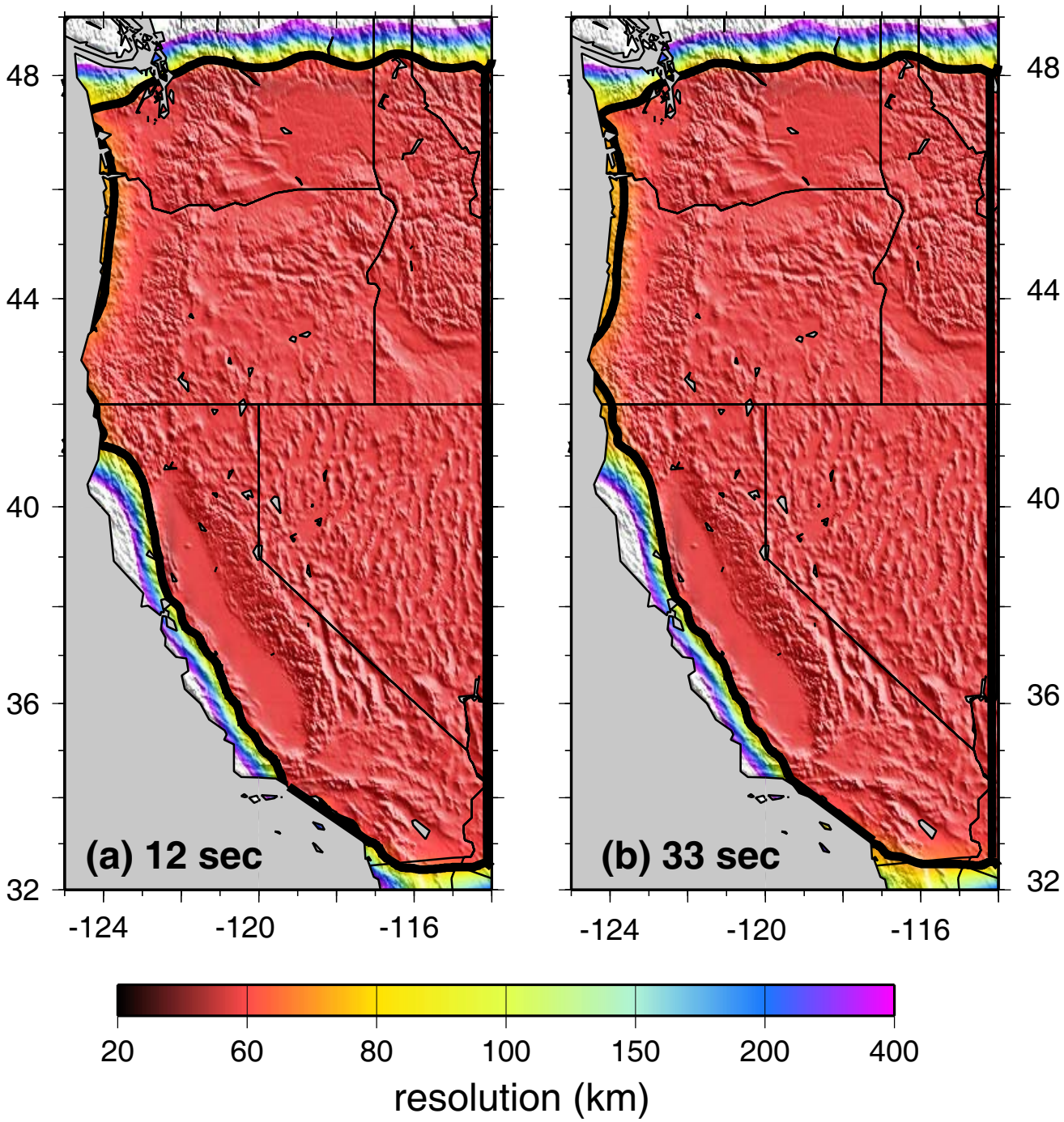
48
44
40
36
32
-124
-120
-116
(a) 12 sec
(b) 33 sec
20
60
80
100
150
200
400
resolution (km)

Figure2

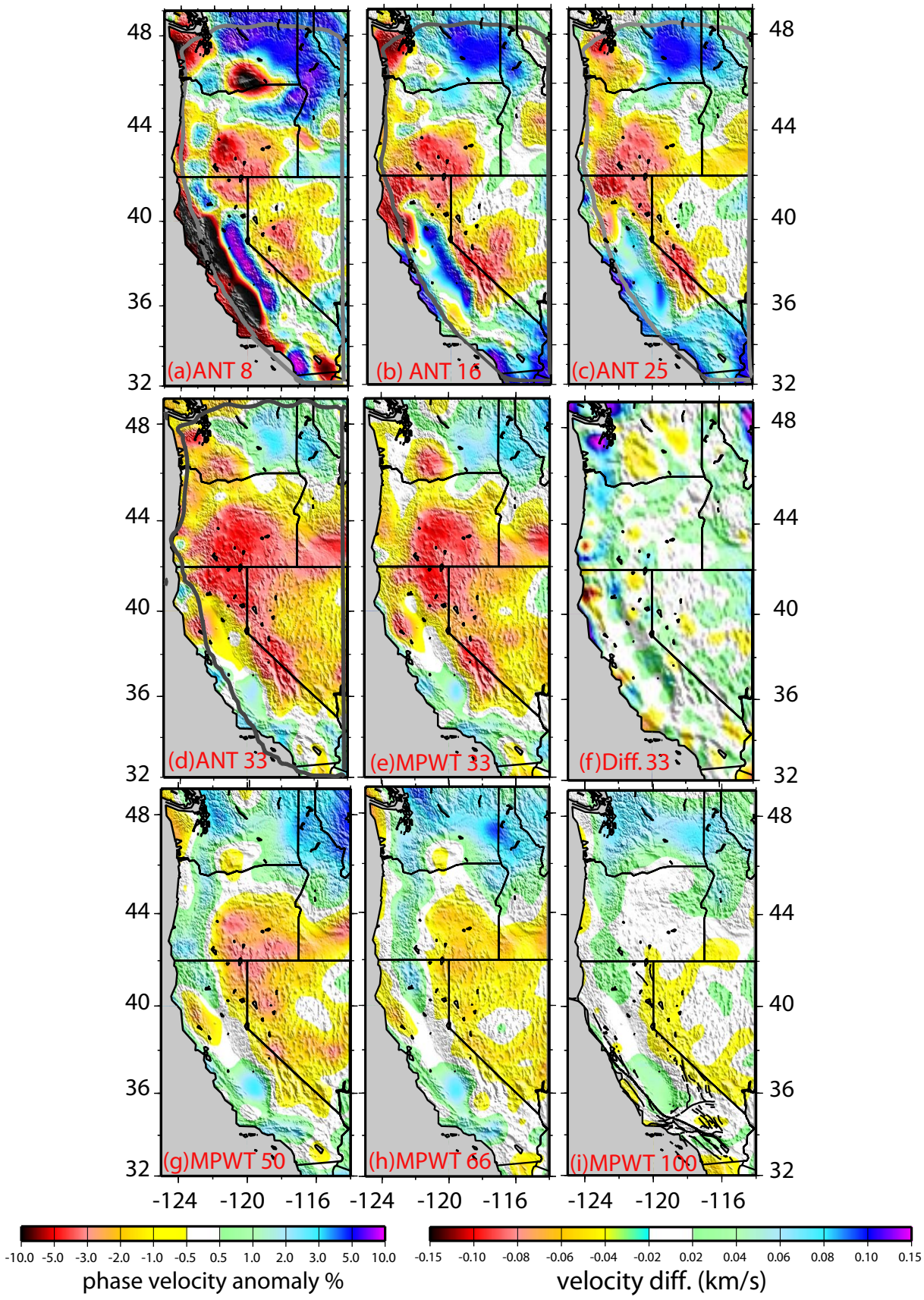
(a)ANT 8
(b) ANT 16
(c)ANT 25
(d)ANT 33
(e)MPWT 33
(f)Diff. 33
(g)MPWT 50
(h)MPWT 66
(i)MPWT 100
48
44
40
36
32
-124
-120
-116
-10.0 -5.0 -3.0 -2.0 -1.0 -0.5 0.5 1.0 2.0 3.0 5.0 10.0
phase velocity anomaly %
-0.15 -0.10 -0.08 -0.06 -0.04 -0.02 0.02 0.04 0.06 0.08 0.10 0.15
velocity diff. (km/s)

Figure 3

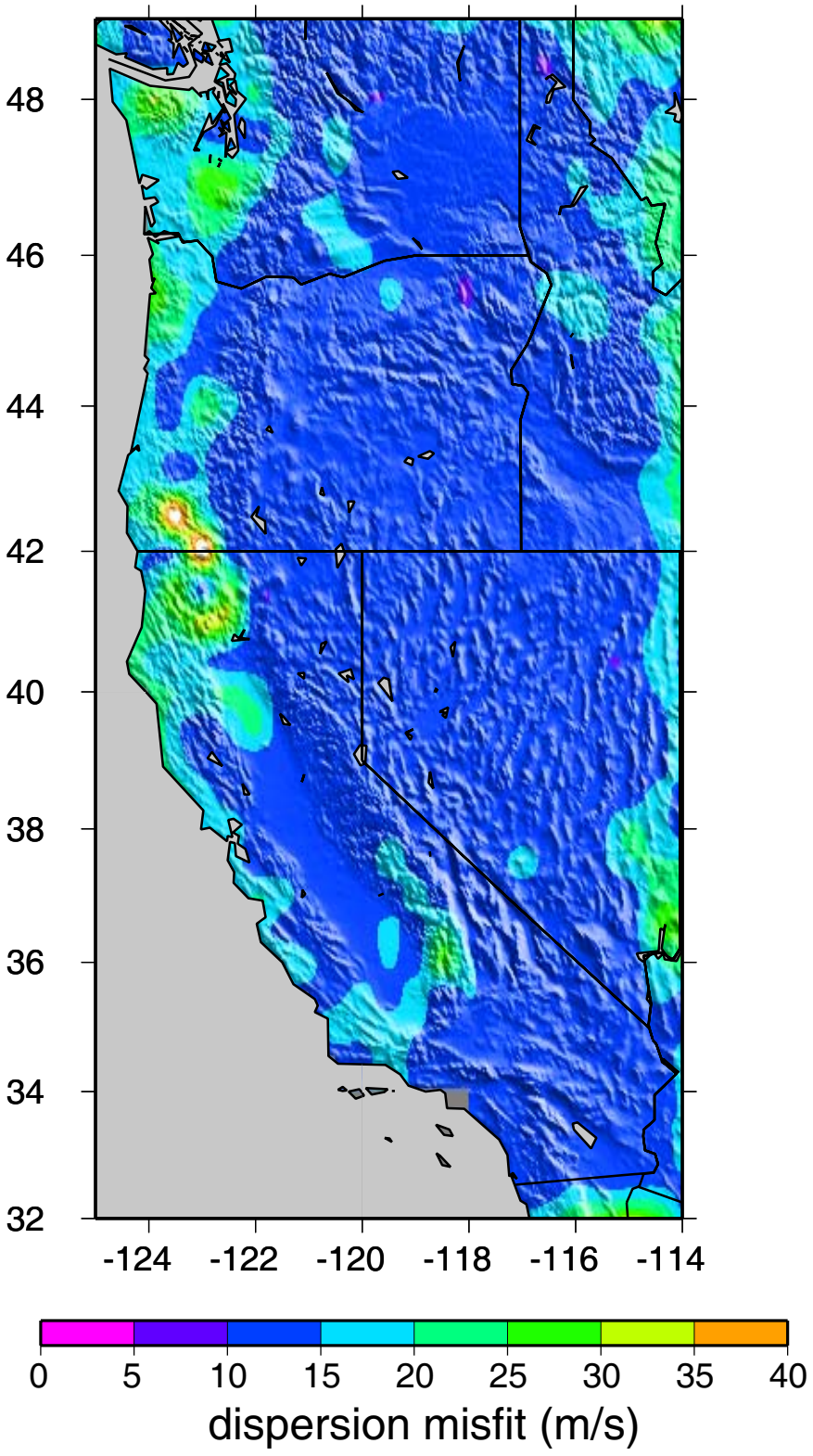
48
46
44
42
40
38
36
34
32
-124
-122
-120
-118
-116
-114
0
5
10
15
20
25
30
35
40
dispersion misfit (m/s)

Figure 4

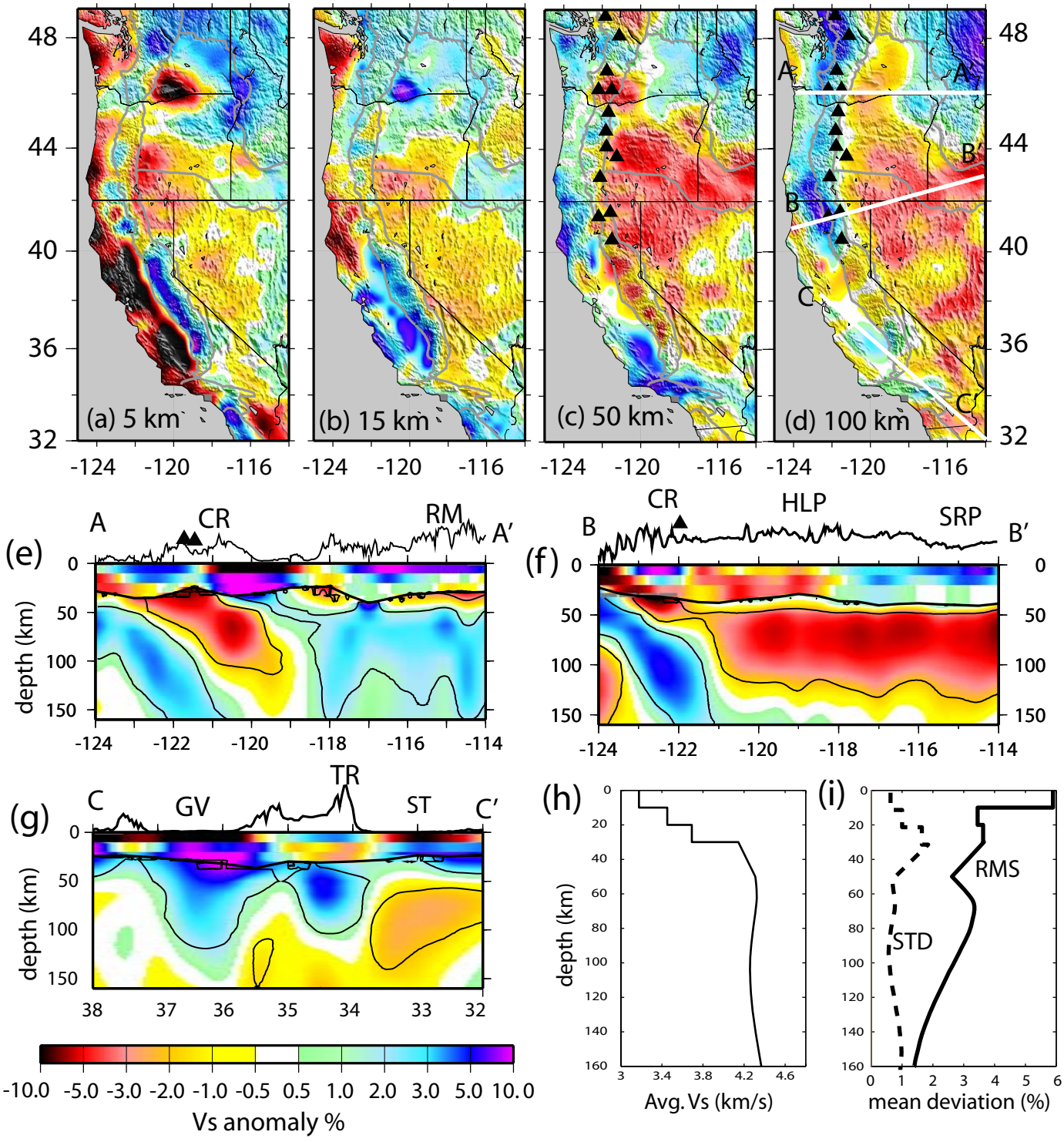
(a) 5 km
(b) 15 km
(c) 50 km
(d) 100 km
A
A′
B
B′
C
C′
48
44
40
36
32
-124
-120
-116
(e)
CR
RM
depth (km)
0
50
100
150
-124
-122
-120
-118
-116
-114
(f)
HLP
SRP
(g)
TR
GV
ST
38
37
36
35
34
33
32
-10.0 -5.0 -3.0 -2.0 -1.0 -0.5 0.5 1.0 2.0 3.0 5.0 10.0
Vs anomaly %
(h)
Avg. Vs (km/s)
(i)
RMS
STD
mean deviation (%)

Figure 5

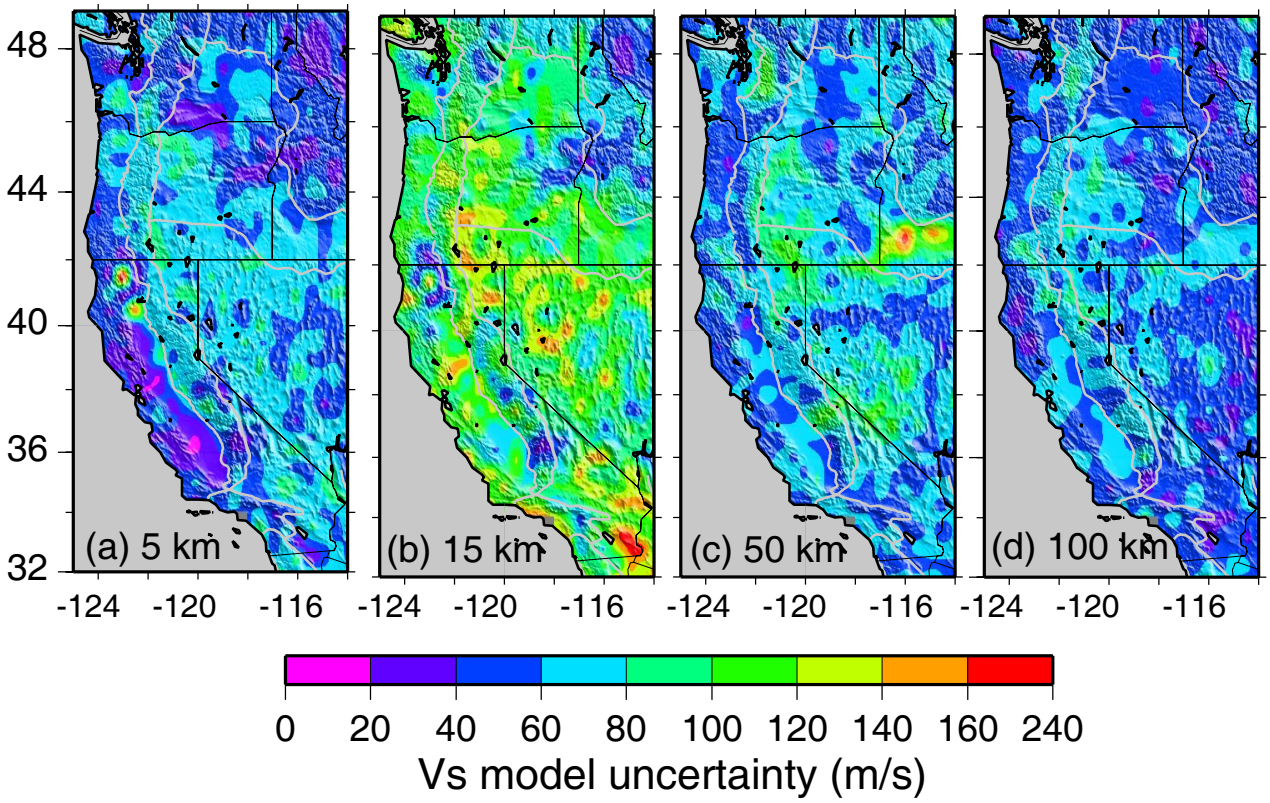
48
44
40
36
32
-124
-120
-116
(a) 5 km
(b) 15 km
(c) 50 km
(d) 100 km
0
20
40
60
80
100
120
140
160
240
Vs model uncertainty (m/s)

Figure 6

P